Geophysical Research Letters

RESEARCH LETTER
10.1029/2023GL107224

Strong Localized Pumping of Water Vapor to High Altitudes on Mars During the Perihelion Season

A. Brines[1], M. A. López-Valverde[1], B. Funke[1], F. González-Galindo[1], S. Aoki[2,3], G. L. Villanueva[4], J. A. Holmes[5], D. A. Belyaev[6], G. Liuzzi[4,7], I. R. Thomas[2], J. T. Erwin[2], U. Grabowski[8], F. Forget[9], J. J. Lopez-Moreno[1], J. Rodriguez-Gomez[1], F. Daerden[2], L. Trompet[2], B. Ristic[2], M. R. Patel[5], G. Bellucci[10], and A. C. Vandaele[2]

[1]Instituto de Astrofísica de Andalucía (IAA/CSIC), Granada, Spain, [2]Royal Belgian Institute for Space Aeronomy, Brussels, Belgium, [3]Department of Complexity Science and Engineering, University of Tokyo, Kashiwa, Japan, [4]NASA Goddard Space Flight Center, Greenbelt, MD, USA, [5]Open University, Milton Keynes, UK, [6]Space Research Institute, Moscow, Russia, [7]American University, Washington, DC, USA, [8]Karlsruhe Institute of Technology, Institute of Meteorology and Climate Research, Karlsruhe, Germany, [9]Laboratoire de Météorologie Dynamique, IPSL, Paris, France, [10]Istituto di Astrofisica e Planetologia, Roma, Italy

Key Points:

- Latitudinal distributions of water vapor up to 120 km are analyzed in detail using Nadir and Occultation for MArs Discovery (NOMAD) observations with an improved retrieval scheme
- Water vapor injection during the perihelion localized around 50°–60°S in three consecutive Martian years
- Martian year 34 Global Dust Storm may have affected the driving mechanisms of the plume, delaying its appearance and reducing its magnitude

Supporting Information:

Supporting Information may be found in the online version of this article.

Correspondence to:

A. Brines,
adrianbm@iaa.es

Citation:

Brines, A., López-Valverde, M. A., Funke, B., González-Galindo, F., Aoki, S., Villanueva, G. L., et al. (2024). Strong localized pumping of water vapor to high altitudes on Mars during the perihelion season. *Geophysical Research Letters*, *51*, e2023GL107224. https://doi.org/10.1029/2023GL107224

Received 13 NOV 2023
Accepted 20 JUN 2024

Abstract Here we present water vapor vertical profiles observed with the ExoMars Trace Gas Orbiter/Nadir and Occultation for MArs Discovery instrument during the perihelion and Southern summer solstice season (L_S = 240°–300°) in three consecutive Martian Years 34, 35, and 36. We show the detailed latitudinal distribution of H_2O at tangent altitudes from 10 to 120 km, revealing a vertical plume at 60°S–50°S injecting H_2O upward, reaching abundance of about 50 ppmv at 100 km. We have observed this event repeatedly in the three Martian years analyzed, appearing at L_S = 260°–280° and showing inter-annual variations in the magnitude and timing due to long term effects of the Martian Year 34 Global Dust Storm. We provide a rough estimate of projected hydrogen escape of 3.2×10^9 cm^{-2} s^{-1} associated to these plumes, adding further evidence of the key role played by the perihelion season in the long term evolution of the planet's climate.

Plain Language Summary Studying the vertical distribution of the Martian atmosphere is crucial to understand what happened to the water presumably present in larger abundance on ancient Mars. We have analyzed the vertical profiles of three Martian Years during the Southern summer, revealing a strong vertical transport of water vapor to the upper atmosphere. This seasonal phenomenon seems to be repeated annually, although with variations in the location and time of the year. Our estimation of the associated upward hydrogen flux represents an important loss which could have contributed to the escape of water to space for at least the period in which Mars had its present orbital inclination.

1. Introduction

The thin atmosphere we observe at Mars nowadays makes the planet cold and dry. In an atmosphere dominated by CO_2, water vapor only represents a small fraction of the total atmospheric composition (~0.03%). Spacecraft observations have provided valuable insights into the H_2O behavior on Mars. In the current Martian climate, H_2O shows a large variability throughout the year involving sublimation and condensation processes affected by dust and atmospheric transport (Montmessin et al., 2017). This cycle is also known to present strong latitudinal gradients, as reported by the Thermal Emission Spectrometer by using column densities (Smith, 2002). However, until the last decade, the knowledge about the water vapor vertical structure and the latitudinal variations at high altitudes was limited. Solar occultation (SO) observations allowed to explore the atmospheric vertical distribution in unprecedented detail. A few instruments, the Spectroscopy for the Investigation of the Characteristics of the Atmosphere of Mars (SPICAM) onboard Mars Express and Auguste onboard the Phobos-2, have provided vertical profiles of the Martian atmosphere using SO observations (Fedorova et al., 2009, 2018, 2021; Maltagliati et al., 2011, 2013) and others, the Compact Reconnaissance Imaging Spectrometer for Mars (CRISM) and the Mars Climate Sounder (MCS), both on board Mars Reconnaissance Orbiter used limb observations for indirect information on H_2O abundance (Clancy et al., 2012, 2017; Heavens et al., 2018).

The first SO and water vapor vertical profiles on Mars were obtained with the Auguste spectrometer (Rodin et al., 1997). With SPICAM and mostly limited to an altitude below 70 km, some of the first dedicated studies on

H_2O vertical profiles were done by Fedorova et al. (2009). Later, Maltagliati et al. (2011, 2013) reported evidence of H_2O present in excess of saturation (supersaturation) during the Northern summer and showed for the first time H_2O vertical profiles during a full MY. They found a strong variability of the profiles and reported discrepancies with General Circulation Models (GCMs). More recently (Fedorova et al., 2021), presented the first multiyear survey of water vapor vertical distribution obtained from SPICAM observations.

Similarly, Clancy et al. (2017) analyzed the seasonal and global variability of H_2O profiles which were derived from CRISM O_2 emission rates. They claimed difficulties in the accuracy of modeling cloud microphysics in Mars GCM simulations.

Later, Fedorova et al. (2018) reported an enhancement of the H_2O abundance in the middle atmosphere during the 2007 dust storm and Chaffin et al. (2017) showed how this led to an increase of the escape rates of hydrogen. this was also studied by Heavens et al. (2018) using estimates of middle atmospheric water vapor and ice content from the distribution of water ice clouds and temperature observed with MCS. This phenomenon was observed again during the 2018 GDS with the Nadir and Occultation for MArs Discovery (NOMAD) and Atmospheric Chemistry Suite (ACS) instruments, both onboard the ExoMars Trace Gas Orbiter (TGO) (Alday et al., 2021; Aoki et al., 2019, 2022; Belyaev et al., 2021; Brines et al., 2023; Fedorova et al., 2020, 2023; Vandaele et al., 2019; Villanueva et al., 2021) and also with the SPICAM instrument, whose observations were compared to the GDS of MY 28 (Fedorova et al., 2021). These recent works analyzed H_2O vertical distribution up to 100 km thanks to the high sensitivity of the instruments.

Aoki et al. (2019), Vandaele et al. (2019), and Fedorova et al. (2020) reported an increase in the H_2O abundance between 40 and 80 km during the GDS, the latter showing dust playing a significant role in altering atmospheric dynamics during dust storms. These events lift dust particles into the atmosphere modifying the temperature profiles due to the dust radiative heating (Neary et al., 2020) and preventing H_2O condensation even at high altitudes, enhancing hydrogen escape (Heavens et al., 2018). Belyaev et al. (2021) presented profiles in the upper mesosphere reporting similar water abundance during the GDS and perihelion periods. Brines et al. (2023) showed the effects of the GDS comparing the southern spring season during MYs 34 and 35 and reported supersaturation events in presence of water ice, a phenomenon also found by Fedorova et al. (2020, 2023). This is in line with the study presented by Poncin et al. (2022), in which on average, large parts of the atmosphere were observed to be close to saturation, although typically at lower altitudes than those observed by Fedorova et al. (2023). Villanueva et al. (2021) reported an increase of the H_2O in both abundance and altitude during the beginning of the Southern summer, but they only retrieved H_2O up to 100 km for one MY and did not focus the analysis on this feature, as done in this paper. This localized phenomenon was studied by Shaposhnikov et al. (2019), who modeled mechanisms responsible for the upward water transport at high southern latitudes during the perihelion season. The injection of water during this season was previously noticed by SPICAM during multi-annual monitoring (Fedorova et al., 2021), where they observed H_2O at high altitudes repeatedly during the Southern summer, confirming a seasonal impact on the hydrogen escape rate.

Here, building upon previous NOMAD water vapor retrievals from Brines et al. (2023), we introduced several improvements which provide H_2O with an optimal vertical resolution from about 10 to 120 km. This work analyzes with an unprecedented detail the vertical distribution of H_2O during the perihelion ($L_S \sim 250°$) and Southern summer solstice ($L_S \sim 270°$) of three consecutive MYs, which besides the dust storms, is claimed to be the season driving the escape of hydrogen to space (Jakosky, 2021; Mayyasi et al., 2023). We focused the analysis on the upper mesosphere, showing for the first time latitudinal structures from 60 to 120 km.

The NOMAD instrument and the data analysis are described in Section 2. In Text S1 in Supporting Information S1 we provide information about the parameterization of the NOMAD SO characterization. Details about the methodology used during the data analysis are presented in Texts S2–S4 in Supporting Information S1. The main results are presented in Section 3. Extended interpretation of the observations and conclusion are given in Sections 4 and 5 respectively. In Text S5 in Supporting Information S1 we show a comparison of three Forward Models (FMs), used to perform an internal validation of the NOMAD characterization and its implementation into the simulations.

2. Data Analysis

The NOMAD instrument is a suite of three spectrometers (channels) covering spectral regions between 0.2 and 4.3 μm. It observes the Martian atmosphere with three channels in different geometries: SO and limb/nadir observation. A third channel observes the atmosphere in both configurations (UVIS). Each channel is equipped with its own set of optics and detectors (Vandaele et al., 2018). The SO channel operates in the infrared covering a spectral range between 2.3 and 4.3 μm (2,320–4,350 cm^{-1}) using an Echelle grating in Littrow configuration with a resolving power around 17,000. NOMAD uses an Acousto-Optical Tunable Filter (AOTF) to separate diffraction orders on the detector plane. In addition, the dispersion and diffraction effects of the light throughout the whole optical system affects the signal reaching the detector introducing an instrumental effect to the spectral lines. Typically, the Instrumental Line Shape (ILS) can be modeled by convolving the monochromatic spectrum with a Gaussian kernel. However, the NOMAD data exhibits an asymmetric ILS with an extended left wing of the Gaussian. This feature can be instead reproduced with a double Gaussian whose separation varies with frequency and diffraction order (Thomas et al., 2022; Villanueva, Liuzzi, Aoki, et al., 2022). More details about the NOMAD AOTF and ILS characterization are summarized in Text S1 in Supporting Information S1.

For this study we selected 1,065 occultations taken with the NOMAD SO channel. The selected observations cover the perihelion and the Southern summer solstice season of three consecutive MYs (34, 35, and 36) with Solar Longitude (L_S) ranging from $L_S = 240°$ to $L_S = 300°$. The seasonal-latitudinal distribution of the occultations is shown in Figure 1e.

We used Level 1 calibrated transmittances processed by the Belgian Institute for Space Aeronomy (BIRA-IASB) (Trompet et al., 2023), which were revised by our in-house pipeline to clean them from residual spectral shifts and bendings at each altitude. The IAA-preprocessing includes the latest NOMAD instrument characterization (Villanueva, Liuzzi, Aoki, et al., 2022) and uses the state-of-the-art line-by-line Karlsruhe Optimized Radiative transfer Algorithm (KOPRA) during the cleaning (Brines et al., 2023; Lopez-Valverde et al., 2022).

For the inversions we selected spectra from the NOMAD diffraction orders 134 (3,011–3,035 cm^{-1}) and 136 (3,056–3,081 cm^{-1}) both containing lines with intensities of about 10^{-21} cm^{-1}/(molecule · cm^{-2}), and from orders 168 (3,775–3,805 cm^{-1}) and 169 (3,798–3,828 cm^{-1}), these two with stronger line intensities of about 10^{-19} cm^{-1}/(molecule · cm^{-2}) from the ν_3 fundamental band. These line intensity and their broadening coefficients used in this study are defined for the standard HITRAN atmosphere (1 atm, 296 K) (Gordon et al., 2022). Although those coefficients are given for air (Earth atmosphere), we performed sensitivity tests comparing KOPRA simulations using the default HITRAN linelist and the list provided by Gamache et al. (2016) for its application to CO_2-rich atmospheres. Our results showed that at the optically thin region of the diffraction orders used in this work, the differences in transmittance between both simulations was below the measurement noise ($<10^{-4}$). Therefore, we decided to use the latest linelist available from Gordon et al. (2022) with standard H_2O line parameters.

Considering this, we used spectra from orders 134 and 136 for the lower atmosphere and from orders 168 and 169 for the upper atmosphere, typically covering an altitude range from 0 to 60 km and from 60 to 120 km respectively. This way, following a similar approach as in Brines et al. (2023) we extended their methodology from two to four diffraction orders using different orders for different altitude ranges in order to avoid optically thick (saturated) absorption lines present in orders 168 and 169 at low altitudes. We improved our retrieval scheme in three ways.

First, we optimized our pipeline in order to handle two diffraction orders simultaneously. Before we were combining two separate inversions, one for each diffraction order, as if they were different measurements. Now, we perform a common global fit of the spectra in the two diffraction orders at once. The selected occultations contain pairs of diffraction orders with at least one of the low altitude orders (134, 136) and one of the high altitude orders (168, 169). This is the optimal way to combine diffraction orders which sample different altitude ranges, avoiding artifacts and ad-hoc assumptions in the transition regions. Details about the combination of orders are presented in Text S2 in Supporting Information S1.

Second, and in support of the previous point, we introduced an automatic selection of the transition region for the merging of the low/high altitude diffraction orders. This is based on a computation of the altitude where the H_2O lines become optically thick, analyzing how the shape of the absorption lines observed by NOMAD changes with altitude in orders 168 and 169.

10.1029/2023GL107224

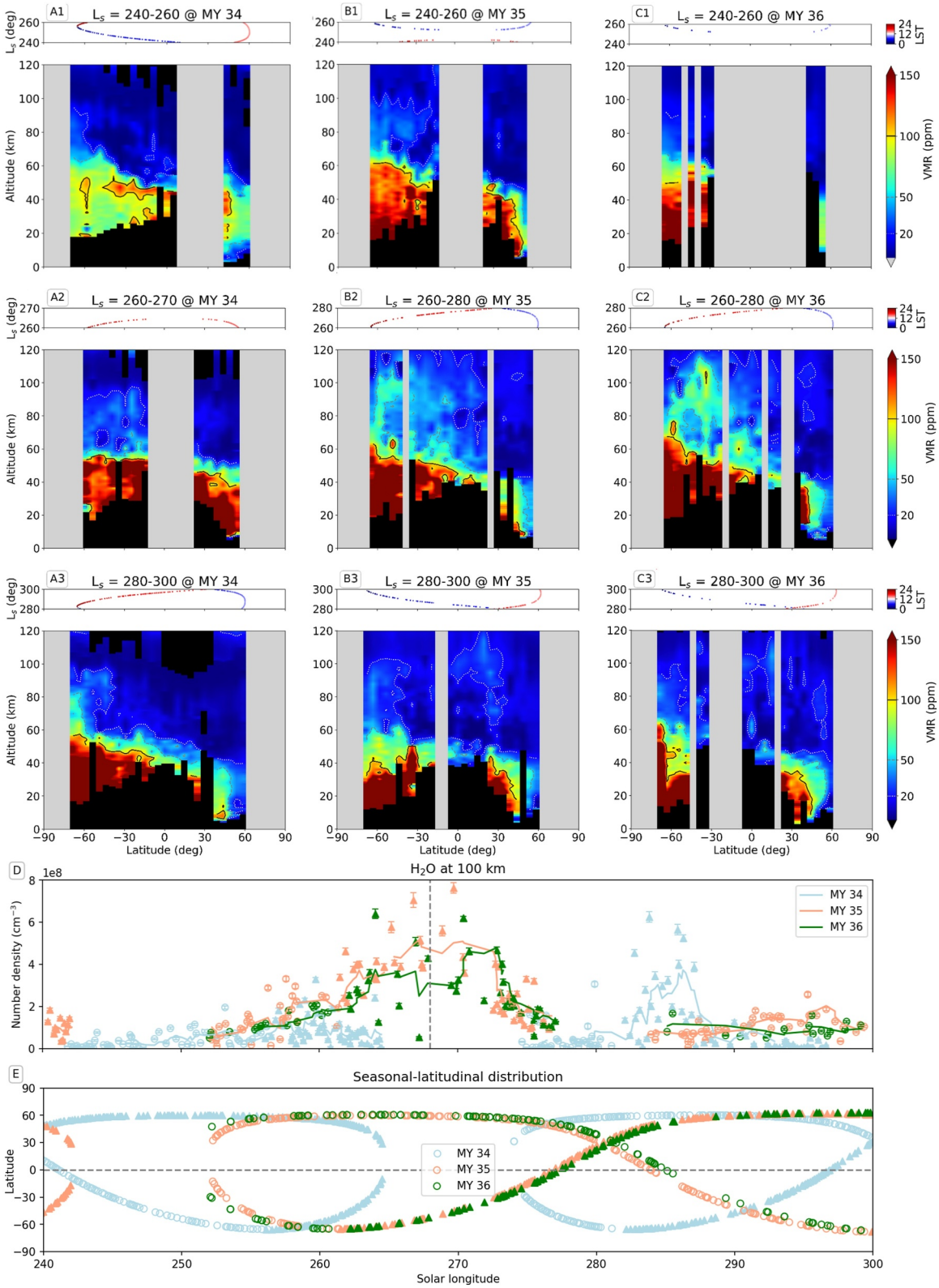

Figure 1.

And third, we developed an in-house tool to improve the characterization of the NOMAD SO measurement noise. This is necessary because our retrieval scheme is optimized to assume the measurement uncertainties as pure uncorrelated random noise. However, the uncertainties provided within the Level 1 calibrated data (Thomas et al., 2022) do not differentiate between systematic and random noise. In order to quantify and correct for the systematic component, we performed an analysis of the spectra at every SO using covariance matrices, allowing us to characterize the random noise of the data. As a result, we are improving the sensitivity and performance of the inversions in the upper atmosphere (90–120 km). A description of the measurement noise characterization is presented in Text S3 in Supporting Information S1.

Using the modification previously described, we managed to improve the retrieved water vapor, obtaining continuous vertical profiles with better vertical resolution compared to the results from Brines et al. (2023), typically ∼2 km (larger than the NOMAD field of view (Vandaele et al., 2018)). Specifically, as shown in Figure S1 (panels F and G) in Supporting Information S1 this improvement can be seen around the transition region from the lower to the upper atmosphere (50–70 km). We performed the inversion of the selected data set following the convergence criteria presented in Brines et al. (2023). The retrievals were performed using the Retrieval Control Program developed at the Institut für Meteorologie und Klimaforschung (IMK) which incorporates KOPRA as FM. For the a priori atmosphere we followed the same approach presented in Brines et al. (2023). That is, during the retrieval process we used total atmospheric densities and temperature-pressure profiles derived from specific runs of the Mars Planetary Climate Model (Forget et al., 1999) developed at the Laboratoire de Météorologie Dynamique (LMD Mars PCM) at the exact location and time of the NOMAD observations. As discussed in Brines et al. (2023), our H_2O retrieval scheme has low sensitivity to changes in temperature profiles. We performed several sensitivity tests in order to estimate the expected errors due to our PCM assumption. Performing retrievals changing the apriori temperature profile by ±5 K had an impact of 2% on the retrieved water vapor VMR while introducing an oscillation in the pressure profile with an amplitude of 10% had an overall impact of less than 4% in the retrieved water vapor number density. During the inversion we used a first order Tikhonov-type regularization optimized for each diffraction order.

A precise FM requires a precise characterization of the instrumental response. Since Brines et al. (2023), we are implementing the latest description of the NOMAD SO (Villanueva, Liuzzi, Aoki, et al., 2022). With the objective of validating this implementation and to unify the criteria used by other teams within the NOMAD consortium, we performed an extensive comparison of the FMs used by the main groups actively analyzing H_2O on Mars with NOMAD SO data. These teams are: Instituto de Astrofísica de Andalucía (IAA-CSIC), Tokyo University, Royal Belgian Institute for Space Aeronomy (ISAB-BIRA), and NASA Goddard Spaceflight Center. This work revealed a remarkable agreement between the FM used by the teams, showing discrepancies below 0.2% when comparing high resolution simulations. A summary is presented in Text S5 in Supporting Information S1.

3. Results

3.1. Latitudinal Variation

The eccentricity of the Martian orbit is known to significantly enhance the solar flux reaching the planet during the perihelion season (Smith et al., 2017), enhancing the wind stress near the surface and the lifting of dust, which in turn absorbs more solar radiation and heats the atmosphere, making the Southern summer ($L_S = 270°–360°$) the warmest and most humid season on Mars. This affects the meridional circulation and vertical transport of water vapor, both being intensified during this season. As mentioned in Section 1, during the perihelion season there are strong gradients in the latitudinal distribution of water column abundance. In order to explore its vertical structure, we studied different L_S periods through the southern spring and summer seasons. We selected observations during

Figure 1. Water vapor latitudinal variation during $L_S^1 = 240°–260°$ (a1, b1, c1), $L_S^2 = 260°–280°$ (a2, b2, c2), and $L_S^3 = 280°–300°$ (a3, b3, c3) for Martian Years (MYs) 34 (left), 35 (middle), and 36 (right). Lines show VMR contours at 100 (black), 50 (gray), and 20 (white) ppmv. Dots in panels a1–a3, b1–b3, c1–c3 indicate the latitude, Solar Longitude, and Local Solar Time of the observations. Panel (d) shows the seasonal variation of water vapor number density (cm^{-3}) in the southern hemisphere at 100 km for $L_S = 240°–300°$ during MYs 34 (blue), 35 (orange), and 36 (green). Vertical dashed line indicates the peak of the plume observed at 100 km during MYs 35 and 36 at $L_S = 268°$. Solid lines show the seasonal average. Panel (e) shows the latitude of the analyzed Nadir and Occultation for MArs Discovery Solar occultation observations over solar longitude for MYs 34 (blue), 35 (orange), and 36 (green). Horizontal dashed line indicates the equator. In panels (d) and (e), morning and evening terminator occultations are indicated with circles and triangles respectively.

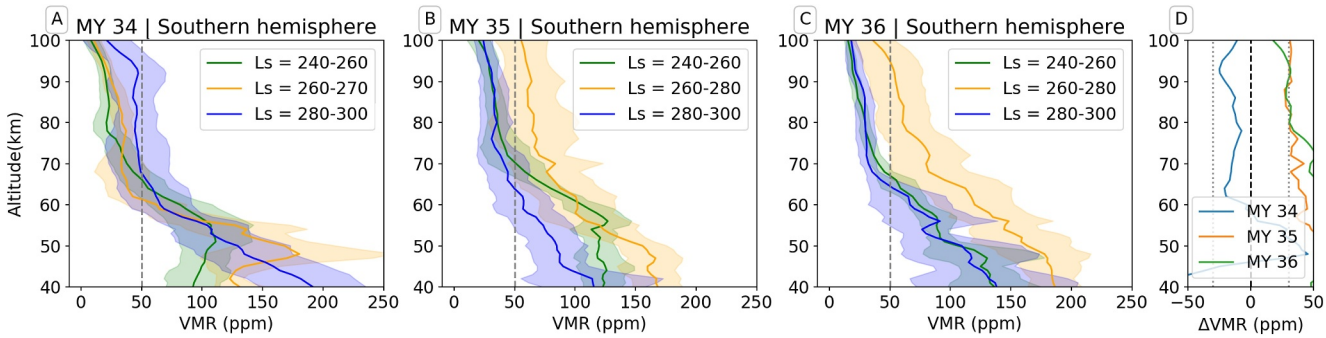

Figure 2. Averaged water vapor VMR profiles at southern hemisphere during solar longitude ranges $L_S^1 = 240° - 260°$ (green), $L_S^2 = 260° - 280°$ (yellow), and $L_S^3 = 280 - 300°$ (blue) for MYs 34(a), 35(b), and 36(c). Profiles from latitudes below 45° have been excluded in the average. Shaded areas represent the standard deviation of the average. Vertical dashed lines indicate abundance of 50 ppmv. Panel (d) shows the averaged profiles difference L_S^2-L_S^3 for MYs 34 (blue), 35 (orange), and 36 (green). Vertical dotted lines indicate abundance of ±30 ppmv (dotted) and 0 ppmv (dashed) for reference.

and after the perihelion season, covering L_S ranges L_S = 240°–260°, L_S = 260°–280°, and L_S = 280°–300° (denoted L_S^1, L_S^2 and L_S^3 respectively) of MYs 34, 35, and 36. The latitudinal distribution of H_2O is presented in Figure 1. We have binned the retrieved profiles in 5° latitude intervals. The bins were calculated with a weighted average of all the profiles within the interval, according to its retrieved uncertainty. Due to the TGO orbital configuration, the L_S^2 range of MY 34 observations is different from the range selected for MYs 35 and 36. The selected ranges optimize the latitudinal coverage. During these L_S periods, we observed a vertical column of H_2O (denoted as "plume") with abundance of about 50 ppmv at 60°S–30°S reaching altitudes up to 100 km during L_S^2 in MYs 35 and 36 (Figures 1b2 and 1c2). MY 34 also showed a similar structure but with reduced abundance and with a peak showing up later in time (Figures 1a3 and 1d). In the three MYs, NOMAD observations do not reveal any significant water injection above 80 km prior to $L_S \sim 260°$ (Figures 1a1, 1b1, and 1c1). In the Northern hemisphere, the H_2O obtained is mostly confined below 40 km and at low-mid latitudes, as expected during the winter season (Montmessin et al., 2017).

We compared our H_2O results with data derived from ACS MIR observations obtained during L_S^2 and L_S^3 in MYs 34 and 35 (Belyaev et al., 2021), revealing a good agreement between both instruments. This is presented in Figure S4 in Supporting Information S1, showing the H_2O number density seasonal variation observed with NOMAD and ACS at 80 and 100 km.

3.2. Interannual Variability

Although we found a strong injection of water vapor to high altitudes in the three MYs, we observed some differences between them. In order to evaluate the contribution of the injection and its interannual variability, we averaged the retrieved profiles within the solar longitude ranges L_S^1, L_S^2, and L_S^3 for each analyzed MY, excluding observations from latitudes below 45° in order to capture vertical profiles representative of the observed plume. The average H_2O profiles for each L_S range in the southern hemisphere are presented in Figure 2 for MYs 34 (A), 35 (B), and 36 (C). The difference in ppmv between L_S^2 and L_S^3 profiles is shown in panel D. We observed a clear enhancement of the water abundance above 80 km of about 30 ppmv during L_S^2 in MYs 35 and 36 (orange and green lines), showing a similar vertical structure in both years. In contrast, MY 34 shows an enhancement of about 15 ppm during L_S^3 due to the peak observed around $L_S \sim 285°$. The vertical profiles observed during the period L_S^1 (green line) prior to the plume detection show a similar trend in the three MYs.

4. Discussion

Recent works reporting TGO SO measurements found high water vapor abundance during the season analyzed here. Belyaev et al. (2021), using the ACS MIR channel found peaks of about 10–30 ppmv of H_2O at 100–120 km around Mars perihelion in MYs 34 and 35; as well as (Fedorova et al., 2023), where the maximum was found up to 100 km. Using NOMAD SO data, Aoki et al. (2022) observed a maximum H_2O density at $L_S = 265°$ in MY 35; Brines et al. (2023) using NOMAD SO observations showed H_2O abundance about 50 ppmv at high altitudes

around $L_S \sim 260°$ in MY 35 and Villanueva et al. (2021), again exploiting NOMAD SO measurements during MYs 34 and 35 denominated this feature as "Aspirator." We report here a detailed latitudinal structure of this phenomenon during three consecutive MYs for the first time, with a robust characterization of the observations in the upper mesosphere (>100 km) and revealing a large H_2O column located at 60°S reaching altitudes up to 110 km. This plume appears during MYs 34, 35, and 36 (Figures 1a–1c respectively), suggesting a large water injection of about 50 ppmv into the upper atmosphere repeatedly every year during a specific period of time $\left(L_S^2\right)$. Observations prior to $L_S = 260° \left(L_S^1\right)$ do not show any significant injection but a gradual increase in water vapor in southern latitudes starting around $L_S = 250°$, specially during MYs 35 and 36 (Figure 1d). However, in MY 34 this phenomenon is observed later in time $\left(L_S^3\right)$ and presents a lower abundance plume, with 50 ppmv at 80 km and <20 ppmv at 100 km (Figure 1a3). This feature, reaching altitudes close to the mesopause (~120 km), can not be simulated by the current LMD Mars PCM (Forget et al., 1999), which was used to generate the apriori climatology used during the retrievals presented here. However, it seems to coincide in time and location with an upward H_2O flux branch in the model by Shaposhnikov et al. (2019). Nonetheless, simulations using data assimilation (DA) (Holmes et al., 2022) showed the presence of the plume during L_S^2 of MY 35. The assimilation combined the Mars PCM Uk-spectral with several spacecraft data sets, including NOMAD water vapor column abundance (Crismani et al., 2021) and NOMAD + ACS water vapor profiles (Alday et al., 2021; Aoki et al., 2019; Fedorova et al., 2020; Villanueva et al., 2021), proving the advantages of combining GCM models with observations. Regardless of this result, firm conclusions about the nature of this feature cannot be drawn solely from DA studies. Future studies with a free GCM focusing on exploring its response to diverse parameters' perturbations shall provide valuable information about the drivers of this unique feature. Data assimilation profiles are shown in Figure S8 in Supporting Information S2.

The discrepancy between MYs 35, 36, and MY 34 might be attributed to several reasons. One is related to the NOMAD sampling and its orbital configuration. The TGO coverage during MY 34 is different compared to the sampling during MYs 35 and 36, this is, TGO sampled the same latitudes at different L_S. If the plume had a preferential latitude to appear every year, NOMAD would not observe it at the same L_S during MY 34 than during MYs 35 and 36. This suggests the H_2O injection observed here to be a local and a short duration phenomenon taking place in a specific time and location. This difference between MY 34 and the following Mars Years is observed in Figure 1d, where the peak of the plume in MYs 35 and 36 occurs at $L_S \sim 268°$, a period of time which was not sampled by TGO during MY 34. Aoki et al. (2022) also reported a H_2O peak at $L_S = 265°$ during MY 35 but not in MY 34, attributing this to differences in the NOMAD sampling.

Another possible cause of the interannual variability may be the alteration of the atmospheric dynamics and transport caused by the MY 34 GDS and its slow decay phase in southern extratropic latitudes at $L_S \sim 255°$ (Kass et al., 2020). The water vapor abundance peak observed later in time at $L_S \sim 285°$ suggests a delay in the appearance of the plume during MY 34. In addition, the abundance below 60 km during MY 34 in the southern hemisphere prior to $L_S = 260°$ show smaller values than in MYs 35 and 36. This circumstance can be observed also in Aoki et al. (2022) (see their Figures 8 and 9), although they did not discuss this interannual difference. Fedorova et al. (2023) also reported much higher water vapor saturation during the perihelion of MY 35 compared to MY 34 and our observations are also compatible with Pankine et al. (2023). They studied the water vapor in the Southern Polar Region (SPR) analyzing observations of several instruments during years with and without global dust events, claiming that water vapor column abundance decreased following the GDS, when compared to years without a GDS. During the period L_S^1, the temperature (Fedorova et al., 2023) and the column dust optical depth (Martín-Rubio et al., 2024) at high southern latitudes where similar in both MY 34 and 35 (see their Figures 2 and 7 respectively), which may exclude the possibility of an enhanced water vapor condensation during the GDS year. Hence, the cause of the water abundance deficit during MY 34 may be related to a lower water vapor production rate by sublimation of the H_2O ice reservoirs. Due to the GDS, the southern polar vortex diminished its intensity during $L_S = 200°$–$220°$, providing a weaker barrier to transport into the SPR and onto the surface (Streeter et al., 2021). This phenomena, could have increased the deposition of dust over H_2O ice during the GDS peak activity, leading to a reduction of the water vapor production rate (Gundlach et al., 2011). Pankine et al. (2023) also suggested the disruption of the southward transport of vapor by the atmospheric circulation as a potential cause of the observed differences between GDS and non-GDS years.

These observations may suggest that, in addition to the strong upward branch of the meridional circulation (Shaposhnikov et al., 2019), the mechanisms driving the formation of the plume require a sufficiently high

tropospheric (<50 km) water vapor abundance at least larger than 100 ppm. In MY 34 this condition is fulfilled during L_S^2, leading to the delayed plume observed during L_S^3. This hypothesis should be explored in future studies with the help of observations from multiple instruments combined with GCMs (Holmes et al., 2022). Note that the measurements during L_S^2 of MYs 35 and 36 correspond to the evening terminator, whereas the measurements during L_S^3 of these same years correspond the morning terminator. This can be observed in Figure 1d, where the peak in H_2O density at $L_S \sim 285°$ only in MY 34 appears during evening observations. At present, we can not exclude local time effects as partially responsible for the plume origin and variability.

In addition to the vertical transport of H_2O in the plume, effects of the meridional transport toward Northern latitudes at high altitudes can also be observed in Figures 1b2 and 1c2, showing a layer of H_2O at 100 km with abundance >20 ppmv reaching latitudes of about 30°N. As the Southern summer advances and the vertical transport around 60°S weakens, the ascending plume vanishes and the vertical and meridional injections of water diminishes. This effect is observed in panels B3 and C3 of Figure 1, where abundance at high altitudes decrease in both hemispheres, suggesting a less efficient northward transport.

Average H_2O profiles in Figure 2 present an enhancement of water above 50 km in the southern hemisphere during L_S^2 of MYs 35 and 36. As seen in panels B and C of Figure 2, it appears repeatedly in both years, showing a difference of 20–30 ppmv at 100 km between the two analyzed L_S periods. In contrast, in Figure 2a this difference is smaller during MY 34, with larger abundance during L_S^3 and showing a variation of about 15 ppmv above 80 km between both L_S ranges. We can use these averaged profiles to estimate the atomic hydrogen escape flux associated to the plumes studied here. Applying the model by Chaffin et al. (2017) and assuming that the water injection from Figures 2b and 2c is sustained during the whole period when the plume is observed (~20° in L_S, i.e. 10^6 s), we obtained an integral escape flux about $\sim 3.2 \pm 0.5 \times 10^9$ cm^{-2} s^{-1}, which is in a similar range as previous results (Belyaev et al., 2021; Bhattacharyya et al., 2017; Holmes et al., 2021). Repeating this exercise for the period when the plume was not observed, we obtained an estimation of $\sim 2.5 \pm 0.3 \times 10^9$ cm^{-2} s^{-1}. Taking into account the uncertainties introduced in the estimation of the escape (~15%) and the possible bias due to the uncertainties of the thermal structure within the region where the profiles where averaged (~5% as a conservative value obtained from our sensitivity tests), we estimate a rough increase by ~30 ± 25% in the hydrogen escape over the period without the plume, which represents a modest but not negligible increase marginally above our uncertainties. Details about the method used for the estimation are presented in Text S4 in Supporting Information S1. This estimation contains several uncertainties and the calculation presented here is only suitable to provide a rough order of magnitude estimate. Testing the known or unknown approximations in Chaffin et al. (2017) photochemical model was not a target of the present work. More recently, Montmessin et al. (2022) used a hybrid photochemistry-transport model combined with ACS observations from Belyaev et al. (2021) to compare the hydrogen escape rate during the perihelion season of MYs 34 and 35, suggesting this season to dominate the long term escape.

5. Conclusions

During perihelion, suspended dust particles alter the thermal structure and consequently the atmospheric dynamics. This directly affects the atmospheric composition by strong vertical transport of minor species like H_2O. This work provides an insight into the water vapor vertical distribution during the perihelion and Southern summer solstice season. We have presented detailed latitudinal variation of the H_2O showing a strong pumping of water into the upper atmosphere and revealing abundance with volume mixing ratios of about 50 ppmv at 100 km. The water vapor plume is observed to be confined to the southern hemisphere at latitudes between 60° and 50°. In addition, we have observed this feature only during a short period of time (20° in L_S) but repeated during the three MYs analyzed here. During non-GDS years we observe the injection to occur at $L_S = 260°–280°$. However, during MY 34 the plume appears shifted toward southern latitudes and appears later in time, showing lower abundance above 80 km. We attributed these differences to variations in the latitudinal and seasonal sampling of the TGO spacecraft and to possible long term effects of the MY 34 GDS weakening the southern polar vortex and allowing the dust to deposit over water ice reservoirs, leading to a reduced water vapor production rate during the perihelion. In order to answer these questions, more observations of this phenomenon will be necessary. Increasing the number of H_2O dedicated observations with TGO during the perihelion season could help to provide a better temporal and latitudinal sampling of this short term and local event. We are planning to learn about possible drivers of this phenomenon by exploring the response of the Mars PCM to diverse parameters'

perturbations, study that will be presented in future works. Finally, we provided a rough estimation of the hydrogen escape flux associated to the strong plumes in MY35 and 36 of about $\sim 3.2 \pm 0.5 \times 10^9$ cm^{-2} s^{-1}, which adds to the importance of the perihelion season to the global budget of hydrogen escape on Mars. The accumulation of more MYs of observations may give us a good estimate of the importance of these plumes over the global and annual hydrogen escape on Mars. Our results are in line with those presented in previous similar analysis. A comparison with Belyaev et al. (2021) presented in Supporting Information S1 shows a good agreement in the H_2O abundance retrieved with NOMAD and ACS instruments, complementing and confirming many of Belyaev et al. (2021) findings with a different instrument and retrieval approach.

Data Availability Statement

The NOMAD SO Level 1a calibrated data used in this work are available at the ESA Planetary Science Archive (PSA, 2024). More information about the data on the PSA can be found in the NOMAD Experiment-to-Archive Interface Control Document (EAICD, 2024). The results retrieved from the NOMAD SO measurements presented in this work are being archived and available at (Brines et al., 2024).

Acknowledgments
The IAA/CSIC team acknowledges financial support from the Severo Ochoa grant CEX2021-001131-S and by grants PID2022-137579NB-I00, RTI2018-100920-J-I00 and PID2022-141216NB-I00 all funded by MCIN/AEI/https://doi.org/10.13039/501100011033. A. Brines acknowledges financial support from the grant PRE2019-088355 funded by MCIN/AEI/https://doi.org/10.13039/501100011033 and by "ESF Investing in your future." ExoMars is a space mission of the European Space Agency (ESA) and Roscosmos. The NOMAD experiment is led by the Royal Belgian Institute for Space Aeronomy (IASB-BIRA), assisted by Co-PI teams from Spain (IAA-CSIC), Italy (INAF-IAPS), and the United Kingdom (Open University). This project acknowledges funding by the Belgian Science Policy Office (BELSPO), with the financial and contractual coordination by the ESA Prodex Office (PEA 4000103401, 4000121493), by Spanish Ministry of Science and Innovation (MCIU) and by European funds under grants PGC2018-101836-B-I00 and ESP2017-87143-R (MINECO/FEDER), as well as by UK Space Agency through grants ST/V002295/1, ST/V005332/1, ST/Y000234/1 and ST/X006549/1 and Italian Space Agency through Grant 2018-2-HH.0. This project has received funding from the European Union's Horizon 2020 research and innovation program under grant agreement No 101004052. US investigators were supported by the National Aeronautics and Space Administration. Canadian investigators were supported by the Canadian Space Agency. We want to thank M. Vals, F. Montmessin, F. Lefevre and the broad team supporting the continuous development of the Mars PCM.

References

Alday, J., Trokhimovskiy, A., Irwin, P. G., Wilson, C. F., Montmessin, F., Lefèvre, F., et al. (2021). Isotopic fractionation of water and its photolytic products in the atmosphere of mars. *Nature Astronomy*, *5*(9), 943–950. https://doi.org/10.1038/s41550-021-01389-x

Aoki, S., Vandaele, A., Daerden, F., Villanueva, G., Liuzzi, G., Thomas, I., et al. (2019). Water vapor vertical profiles on Mars in dust storms observed by TGO/NOMAD. *Journal of Geophysical Research: Planets*, *124*(12), 3482–3497. https://doi.org/10.1029/2019je006109

Aoki, S., Vandaele, A. C., Daerden, F., Villanueva, G. L., Liuzzi, G., Clancy, R. T., et al. (2022). Global vertical distribution of water vapor on Mars: Results from 3.5 years of ExoMars-TGO/NOMAD science operations.

Belyaev, D. A., Fedorova, A., Trokhimovskiy, A., Alday, J., Montmessin, F., Korablev, O. I., et al. (2021). Revealing a high water abundance in the upper mesosphere of Mars with ACS onboard TGO. *Geophysical Research Letters*, *48*(10), e2021GL093411. https://doi.org/10.1029/2021gl093411

Bhattacharyya, D., Clarke, J., Chaufray, J.-Y., Mayyasi, M., Bertaux, J.-L., Chaffin, M., et al. (2017). Seasonal changes in hydrogen escape from mars through analysis of HST observations of the Martian exosphere near perihelion. *Journal of Geophysical Research: Space Physics*, *122*(11), 11–756. https://doi.org/10.1002/2017ja024572

Brines, A., López-Valverde, M., Funke, B., Galindo, F., Aoki, S., Villanueva, G., et al. (2024). Strong localized pumping of water vapor to high altitudes on Mars during the perihelion season [Dataset]. *Zenodo*. https://doi.org/10.5281/zenodo.10779225

Brines, A., López-Valverde, M., Stolzenbach, A., Modak, A., Funke, B., Galindo, F., et al. (2023). Water vapor vertical distribution on mars during perihelion season of my 34 and MY 35 with exomars-tgo/nomad observations. *Journal of Geophysical Research: Planets*, *128*(11), e2022JE007273. https://doi.org/10.1029/2022je007273

Chaffin, M., Deighan, J., Schneider, N., & Stewart, A. (2017). Elevated atmospheric escape of atomic hydrogen from mars induced by high-altitude water. *Nature Geoscience*, *10*(3), 174–178. https://doi.org/10.1038/ngeo2887

Clancy, R. T., Sandor, B. J., Wolff, M. J., Smith, M. D., Lefèvre, F., Madeleine, J.-B., et al. (2012). Extensive MRO CRISM observations of 1.27 μm O_2 airglow in mars polar night and their comparison to MRO MCS temperature profiles and LMD GCM simulations. *Journal of Geophysical Research*, *117*(E11). https://doi.org/10.1029/2011je004018

Clancy, R. T., Smith, M. D., Lefèvre, F., McConnochie, T. H., Sandor, B. J., Wolff, M. J., et al. (2017). Vertical profiles of mars 1.27 μm o2 dayglow from MRO CRISM limb spectra: Seasonal/global behaviors, comparisons to LMDGCM simulations, and a global definition for mars water vapor profiles. *Icarus*, *293*, 132–156. https://doi.org/10.1016/j.icarus.2017.04.011

Crismani, M., Villanueva, G., Liuzzi, G., Smith, M., Knutsen, E., Daerden, F., et al. (2021). A global and seasonal perspective of martian water vapor from exomars/nomad. *Journal of Geophysical Research: Planets*, *126*(11), e2021JE006878. https://doi.org/10.1029/2021je006878

EAICD. (2024). EAICD [Dataset]. *European Space Agency*. Retrieved from https://archives.esac.esa.int/psa/ftp/ExoMars2016/em16_tgo_nmd/document/EAICD/

Fedorova, A., Bertaux, J.-L., Betsis, D., Montmessin, F., Korablev, O., Maltagliati, L., & Clarke, J. (2018). Water vapor in the middle atmosphere of Mars during the 2007 global dust storm. *Icarus*, *300*, 440–457. https://doi.org/10.1016/j.icarus.2017.09.025

Fedorova, A., Korablev, O., Bertaux, J.-L., Rodin, A., Montmessin, F., Belyaev, D., & Reberac, A. (2009). Solar infrared occultation observations by spicam experiment on mars-express: Simultaneous measurements of the vertical distributions of H_2O, CO_2 and aerosol. *Icarus*, *200*(1), 96–117. https://doi.org/10.1016/j.icarus.2008.11.006

Fedorova, A., Montmessin, F., Korablev, O., Lefèvre, F., Trokhimovskiy, A., & Bertaux, J.-L. (2021). Multi-annual monitoring of the water vapor vertical distribution on mars by spicam on mars express. *Journal of Geophysical Research: Planets*, *126*(1), e2020JE006616. https://doi.org/10.1029/2020je006616

Fedorova, A., Montmessin, F., Korablev, O., Luginin, M., Trokhimovskiy, A., Belyaev, D. A., et al. (2020). Stormy water on Mars: The distribution and saturation of atmospheric water during the dusty season. *Science*, *367*(6475), 297–300. https://doi.org/10.1126/science.aay9522

Fedorova, A., Montmessin, F., Trokhimovskiy, A., Luginin, M., Korablev, O., Alday, J., et al. (2023). A two-Martian years survey of the water vapor saturation state on mars based on ACS NIR/TGO occultations. *Journal of Geophysical Research: Planets*, *128*(1), e2022JE007348. https://doi.org/10.1029/2022je007348

Forget, F., Hourdin, F., Fournier, R., Hourdin, C., Talagrand, O., Collins, M., et al. (1999). Improved general circulation models of the Martian atmosphere from the surface to above 80 km. *Journal of Geophysical Research*, *104*(E10), 24155–24175. https://doi.org/10.1029/1999je001025

Gamache, R. R., Farese, M., & Renaud, C. L. (2016). A spectral line list for water isotopologues in the 1100–4100 cm- 1 region for application to co2-rich planetary atmospheres. *Journal of Molecular Spectroscopy*, *326*, 144–150. https://doi.org/10.1016/j.jms.2015.09.001

Gordon, I. E., Rothman, L. S., Hargreaves, R., Hashemi, R., Karlovets, E. V., Skinner, F., et al. (2022). The HITRAN2020 molecular spectroscopic database. *Journal of quantitative spectroscopy and radiative transfer*, *277*, 107949. https://doi.org/10.1016/j.jqsrt.2021.107949

Gundlach, B., Skorov, Y. V., & Blum, J. (2011). Outgassing of icy bodies in the solar system—I. the sublimation of hexagonal water ice through dust layers. *Icarus*, *213*(2), 710–719. https://doi.org/10.1016/j.icarus.2011.03.022

Heavens, N. G., Kleinböhl, A., Chaffin, M. S., Halekas, J. S., Kass, D. M., Hayne, P. O., et al. (2018). Hydrogen escape from Mars enhanced by deep convection in dust storms. *Nature Astronomy*, *2*(2), 126–132. https://doi.org/10.1038/s41550-017-0353-4

Holmes, J., Lewis, S., Patel, M., Alday, J., Aoki, S., Liuzzi, G., et al. (2022). Global variations in water vapor and saturation state throughout the mars year 34 dusty season. *Journal of Geophysical Research: Planets*, *127*(10), e2022JE007203. https://doi.org/10.1029/2022je007203

Holmes, J., Lewis, S., Patel, M., Chaffin, M., Cangi, E., Deighan, J., et al. (2021). Enhanced water loss from the martian atmosphere during a regional-scale dust storm and implications for long-term water loss. *Earth and Planetary Science Letters*, *571*, 117109. https://doi.org/10.1016/j.epsl.2021.117109

Jakosky, B. M. (2021). Atmospheric loss to space and the history of water on mars. *Annual Review of Earth and Planetary Sciences*, *49*(1), 71–93. https://doi.org/10.1146/annurev-earth-062420-052845

Kass, D., Schofield, J., Kleinböhl, A., McCleese, D., Heavens, N., Shirley, J., & Steele, L. (2020). Mars climate sounder observation of mars' 2018 global dust storm. *Geophysical Research Letters*, *47*(23), e2019GL083931. https://doi.org/10.1029/2019gl083931

Lopez-Valverde, M. A., Funke, B., Brines, A., Stolzenbach, A., Modak, A., Gonzalez-Galindo, F., et al. (2022). Martian atmospheric temperature and density profiles during the 1st year of NOMAD/TGO solar occultation measurements.

Maltagliati, L., Montmessin, F., Fedorova, A., Korablev, O., Forget, F., & Bertaux, J.-L. (2011). Evidence of water vapor in excess of saturation in the atmosphere of Mars. *Science*, *333*(6051), 1868–1871. https://doi.org/10.1126/science.1207957

Maltagliati, L., Montmessin, F., Korablev, O., Fedorova, A., Forget, F., Määttänen, A., et al. (2013). Annual survey of water vapor vertical distribution and water–aerosol coupling in the Martian atmosphere observed by SPICAM/MEx solar occultations. *Icarus*, *223*(2), 942–962. https://doi.org/10.1016/j.icarus.2012.12.012

Martín-Rubio, C., Vicente-Retortillo, A., Gómez, F., & Rodríguez-Manfredi, J. (2024). Interannual variability of regional dust storms between mars years 24 and 36. *Icarus*, *412*, 115982. https://doi.org/10.1016/j.icarus.2024.115982

Mayyasi, M., Clarke, J., Chaufray, J.-Y., Kass, D., Bougher, S., Bhattacharyya, D., et al. (2023). Solar cycle and seasonal variability of h in the upper atmosphere of mars. *Icarus*, *393*, 115293. https://doi.org/10.1016/j.icarus.2022.115293

Montmessin, F., Belyaev, D. A., Lefèvre, F., Alday, J., Vals, M., Fedorova, A., et al. (2022). Reappraising the production and transfer of hydrogen atoms from the middle to the upper atmosphere of mars at times of elevated water vapor. *Journal of Geophysical Research: Planets*, *127*(5), e2022JE007217. https://doi.org/10.1029/2022je007217

Montmessin, F., Smith, M. D., Langevin, Y., Mellon, M. T., & Fedorova, A. (2017). The water cycle. *The atmosphere and climate of Mars*, *18*, 338–373. https://doi.org/10.1017/9781139060172.011

Neary, L., Daerden, F., Aoki, S., Whiteway, J., Clancy, R. T., Smith, M., et al. (2020). Explanation for the increase in high-altitude water on Mars observed by NOMAD during the 2018 global dust storm. *Geophysical Research Letters*, *47*(7), e2019GL084354. https://doi.org/10.1029/2019gl084354

Pankine, A. A., Leung, C., Tamppari, L., Martinez, G., Giuranna, M., Piqueux, S., et al. (2023). Effects of global dust storms on water vapor in the southern polar region of mars. *Journal of Geophysical Research: Planets*, *128*(12), e2023JE008016. https://doi.org/10.1029/2023je008016

Poncin, L., Kleinböhl, A., Kass, D. M., Clancy, R. T., Aoki, S., & Vandaele, A. C. (2022). Water vapor saturation and ice cloud occurrence in the atmosphere of mars. *Planetary and Space Science*, *212*, 105390. https://doi.org/10.1016/j.pss.2021.105390

PSA. (2024). European space agency [Dataset]. *PSA*. Retrieved from https://archives.esac.esa.int/psa/#!Table%20View/NOMAD=instrument.EuropeanSpaceAgency

Rodin, A., Korablev, O., & Moroz, V. (1997). Vertical distribution of water in the near-equatorial troposphere of mars: Water vapor and clouds. *Icarus*, *125*(1), 212–229. https://doi.org/10.1006/icar.1996.5602

Shaposhnikov, D. S., Medvedev, A. S., Rodin, A. V., & Hartogh, P. (2019). Seasonal water "pump" in the atmosphere of Mars: Vertical transport to the thermosphere. *Geophysical Research Letters*, *46*(8), 4161–4169. https://doi.org/10.1029/2019gl082839

Smith, M. D. (2002). The annual cycle of water vapor on Mars as observed by the Thermal Emission Spectrometer. *Journal of Geophysical Research*, *107*(E11), 25–31. https://doi.org/10.1029/2001je001522

Smith, M. D., Bougher, S. W., Encrenaz, T., Forget, F., & Kleinböhl, A. (2017). Thermal structure and composition. *The atmosphere and climate of Mars*, *18*, 42–75. https://doi.org/10.1017/9781139060172.004

Streeter, P. M., Lewis, S. R., Patel, M. R., Holmes, J. A., Fedorova, A. A., Kass, D. M., & Kleinböhl, A. (2021). Asymmetric impacts on mars' polar vortices from an equinoctial global dust storm. *Journal of Geophysical Research: Planets*, *126*(5), e2020JE006774. https://doi.org/10.1029/2020je006774

Thomas, I. R., Aoki, S., Trompet, L., Robert, S., Depiesse, C., Willame, Y., et al. (2022). Calibration of nomad on ESA'S EXOMARS trace gas orbiter: Part 1–the solar occultation channel. *Planetary and Space Science*, *218*, 105411. https://doi.org/10.1016/j.pss.2021.105411

Trompet, L., Vandaele, A., Thomas, I., Aoki, S., Daerden, F., Erwin, J., et al. (2023). Carbon dioxide retrievals from nomad-so on ESA'S EXOMARS trace gas orbiter and temperature profiles retrievals with the hydrostatic equilibrium equation: 1. Description of the method. *Journal of Geophysical Research: Planets*, *128*(3), e2022JE007277. https://doi.org/10.1029/2022je007277

Vandaele, A. C., Korablev, O., Daerden, F., Aoki, S., Thomas, I. R., Altieri, F., et al. (2019). Martian dust storm impact on atmospheric H_2O and D/H observed by exomars trace gas orbiter. *Nature*, *568*(7753), 521–525. https://doi.org/10.1038/s41586-019-1097-3

Vandaele, A. C., Lopez-Moreno, J.-J., Patel, M. R., Bellucci, G., Daerden, F., Ristic, B., et al. (2018). NOMAD, an integrated suite of three spectrometers for the ExoMars trace gas mission: Technical description, science objectives and expected performance. *Space Science Reviews*, *214*(5), 1–47. https://doi.org/10.1007/s11214-018-0517-2

Villanueva, G. L., Liuzzi, G., Aoki, S. W., Shohei, A. S., Brines, A., Thomas, I. R., et al. (2022). The deuterium isotopic ratio of water released from the Martian caps as measured with TGO/NOMAD.

Villanueva, G. L., Liuzzi, G., Crismani, M. M., Aoki, S., Vandaele, A. C., Daerden, F., et al. (2021). Water heavily fractionated as it ascends on Mars as revealed by ExoMars/NOMAD. *Science Advances*, *7*(7), eabc8843. https://doi.org/10.1126/sciadv.abc8843

References From the Supporting Information

Jiménez-Monferrer, S., López-Valverde, M. Á., Funke, B., González-Galindo, F., Piccialli, A., García-Comas, M., et al. (2021). CO2 retrievals in the Mars daylight thermosphere from its 4.3 μm limb emission measured by OMEGA/MEx. *Icarus*, *353*, 113830. https://doi.org/10.1016/j.icarus.2020.113830

Kuntz, M. (1997). A new implementation of the humlicek algorithm for the calculation of the voigt profile function. *Journal of Quantitative Spectroscopy and Radiative Transfer*, *57*(6), 819–824. https://doi.org/10.1016/s0022-4073(96)00162-8

Liuzzi, G., Villanueva, G. L., Mumma, M. J., Smith, M. D., Daerden, F., Ristic, B., et al. (2019). Methane on Mars: New insights into the sensitivity of CH_4 with the NOMAD/ExoMars spectrometer through its first in-flight calibration. *Icarus*, *321*, 671–690. https://doi.org/10.1016/j.icarus.2018.09.021

Ruyten, W. (2004). Comment on "a new implementation of the humlicek algorithm for the calculation of the voigt profile function" by m. kuntz [jqsrt 57 (6)(1997) 819–824]. *Journal of Quantitative Spectroscopy and Radiative Transfer*, *86*(2), 231–233. https://doi.org/10.1016/j.jqsrt.2003.12.027

Stiller, G. P., von Clarmann, T., Funke, B., Glatthor, N., Hase, F., Höpfner, M., & Linden, A. (2002). Sensitivity of trace gas abundances retrievals from infrared limb emission spectra to simplifying approximations in radiative transfer modelling. *Journal of Quantitative Spectroscopy and Radiative Transfer*, *72*(3), 249–280. https://doi.org/10.1016/s0022-4073(01)00123-6

Vandaele, A. C., De Mazière, M., Drummond, R., Mahieux, A., Neefs, E., Wilquet, V., et al. (2008). Composition of the venus mesosphere measured by solar occultation at infrared on board venus express. *Journal of Geophysical Research*, *113*(E5), E00B22. https://doi.org/10.1029/2008je003140

Vandaele, A. C., Kruglanski, M., & De Mazière, M. (2006). Modeling and retrieval of atmospheric spectra using asimut.

Villanueva, G. L., Liuzzi, G., Faggi, S., Protopapa, S., Kofman, V., Fauchez, T., et al. (2022). Fundamentals of the planetary spectrum generator. Fundamentals of the planetary spectrum generator. In *2022 edition of the handbook by GL Villanueva et al*.

Villanueva, G. L., Smith, M. D., Protopapa, S., Faggi, S., & Mandell, A. M. (2018). Planetary spectrum generator: An accurate online radiative transfer suite for atmospheres, comets, small bodies and exoplanets. *Journal of Quantitative Spectroscopy and Radiative Transfer*, *217*, 86–104. https://doi.org/10.1016/j.jqsrt.2018.05.023

von Clarmann, V., Glatthor, N., Grabowski, U., Höpfner, M., Kellmann, S., Kiefer, M., et al. (2003). Retrieval of temperature and tangent altitude pointing from limb emission spectra recorded from space by the Michelson interferometer for passive atmospheric sounding (MIPAS). *Journal of Geophysical Research*, *108*, D23. https://doi.org/10.1029/2003jd003602